

A QUANTITATIVE STUDY OF SOURCE IMAGING IN RANDOM WAVEGUIDES

LILIANA BORCEA*, JOSSELIN GARNIER† AND CHRYSOULA TSOGKA‡

Abstract. We present a quantitative study of coherent array imaging of remote sources in randomly perturbed waveguides with bounded cross-section. We study how long range cumulative scattering by perturbations of the boundary and the medium impedes the imaging process. We show that boundary scattering effects can be mitigated with filters that enhance the coherent part of the data. The filters are obtained by optimizing a measure of quality of the image. The point is that there is an optimal trade-off between the robustness and resolution of images in such waveguides, which can be found adaptively, as the data are processed to form the image. Long range scattering by perturbations of the medium is harder to mitigate than scattering by randomly perturbed boundaries. Coherent imaging methods do not work and more complex incoherent methods, based on transport models of energy, should be used instead. Such methods are not useful, nor needed in waveguides with perturbed boundaries. We explain all these facts using rigorous asymptotic stochastic analysis of the wave field in randomly perturbed waveguides. We also analyze the adaptive coherent imaging method and obtain a quantitative agreement with the results of numerical simulations.

1. Introduction. We present a theoretical and numerical study of imaging remote sources in random waveguides, using an array of sensors that record acoustic waves. The waveguide effect is caused by the boundary of the cross-section, which traps the waves and guides the energy along the range direction z , as illustrated in Figure 1.1. We restrict our study to two-dimensional waveguides, because the numerical simulations become prohibitively expensive in three dimensions. The results are similar in three-dimensional waveguides with bounded cross-section. We refer to [2] for an analysis of wave propagation and imaging in three-dimensional random waveguides with unbounded cross-section.

Scattering at the boundary creates multiple traveling paths of the waves from the source to the receiver array. Mathematically, we can write the wave field p (the acoustic pressure) as a superposition of a countable set of waveguide modes, which are solutions of the homogeneous wave equation. Finitely many modes propagate in the range direction at different speeds, and the remaining infinitely many modes are evanescent waves that decay exponentially with range. We may associate the propagating modes with planar waves that strike the boundaries at different angles of incidence. The slow modes correspond to near normal incidence. They reflect repeatedly at the boundary, thus traveling a long path to the array. The fast modes correspond to small grazing angles and shorter paths to the array.

In ideal waveguides with straight boundaries and wave speed that is constant or varies smoothly with cross-range, the wave equation is separable and the modes are uncoupled. In particular, each mode has a constant amplitude which is determined by the source excitation. We study perturbed waveguides with small and rapid fluctuations of the boundaries and of the wave speed, due to numerous weak inhomogeneities. Such fluctuations are not known and are of no interest in imaging. However, they cannot be neglected because they cause wave scattering that accumulates over long distances of propagation. To address the uncertainty of the boundary and wave

*Computational and Applied Mathematics, Rice University, Houston, TX 77005. borcea@rice.edu

†Laboratoire de Probabilités et Modèles Aléatoires & Laboratoire Jacques-Louis Lions, Université Paris VII, 75205 Paris Cedex 13, France. garnier@math.univ-paris-diderot.fr

‡Applied Mathematics, University of Crete & IACM/FORTH, 71409 Heraklion, Greece. tsogka@tem.uoc.gr

speed fluctuations, we model them with random processes, and thus speak of random waveguides. The array measures one realization of the random field p , the solution of the wave equation in one realization of the random waveguide. That is to say, for a particular perturbed boundary and medium. When cumulative scattering by the perturbations is significant, the measurements are quite different from those in ideal waveguides. Furthermore, if we could repeat the experiment for many realizations of the perturbations, we would see that the measurements change unpredictably, they are statistically unstable.

The expectation (statistical mean) $\mathbb{E}[p]$ of the wave is called the *coherent* field. This is the part of the data that is useful for coherent imaging, because we can relate it to the unknown location of the source, in spite of the uncertainty of the perturbations in the waveguide. The challenge is to process the data in order to enhance the coherent part $\mathbb{E}[p]$ and mitigate the unwanted reverberations $p - \mathbb{E}[p]$, the *incoherent* part. Coherent methods without such processing give images that are difficult to interpret and unreliable. They change unpredictably with the realization of the random waveguide, they are not statistically stable.

We refer to [1] for a rigorous asymptotic stochastic analysis of the wave field p in waveguides with randomly perturbed boundaries, and to [8, 4, 5, 6] for waveguides with randomly perturbed media. The analysis shows that p can be modeled as a superposition of ideal waveguide modes that are coupled by scattering at the random perturbations. Explicitly, the modes have amplitudes that are random functions of frequency and range, and satisfy a coupled system of stochastic differential equations. Their expectations decay exponentially with range, on mode- and frequency-dependent length scales called *scattering mean free paths*. The decay means that the incoherent fluctuations of the amplitudes gain strength, and once they become dominant, the modes should not be used in coherent imaging.

It is not surprising that the scattering mean free paths are longer for the fast propagating modes than the slower ones. This is because the latter are waves that take longer trajectories from the source to the array, and interact more with the perturbations of the boundaries and the medium. We show in this paper that a successful imaging strategy depends on which perturbations play the dominant role in the waveguide. If scattering from perturbed boundaries dominates, the fast modes have a much longer scattering mean free path than the slower modes. Therefore, the data remain partially coherent at long ranges and we can seek an adaptive imaging approach that detects the slow modes with incoherent amplitudes and suppresses them. The longer the range, the fewer the modes that remain coherent, so there is a trade-off between the statistical stability and the resolution of the images, which can be optimized with the adaptive method.

When we compare the effect of perturbed boundaries to that of perturbed media, for similar amplitude and correlation length of the fluctuations, we find two essential differences: The latter gives much shorter scattering mean free paths for the faster modes, and the rate of change of these scales with the mode index is much slower. There is no trade-off between statistical stability and resolution of coherent images in such waveguides. As the range increases, the mode amplitudes become incoherent on roughly the same range scale, so there is no gain in removing the slow modes. Coherent imaging fails and should be replaced by incoherent methods, based on transport equations for the energy resolved locally in time and over the modes i.e., over the direction of propagation of the associated plane waves. We refer to [3] for an example of incoherent imaging in random waveguides. These methods are more complex and

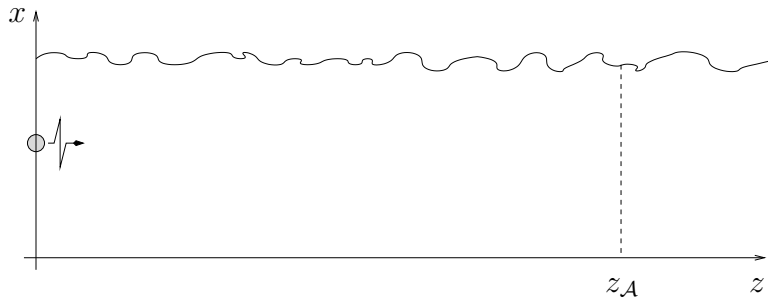


FIG. 1.1. *Schematic of the problem setup. A source emits a signal in a waveguide and the wave field is recorded at a remote array. The waves propagate along the range axis z . The waveguide is bounded in the cross-range direction x . The bottom boundary is rigid and flat. The pressure release top boundary may fluctuate. The system of coordinates has the origin of range at the source. The array is shown on the right of the source, at range z_A .*

computationally involved than the coherent ones. They are designed to work at ranges that exceed the scattering mean free paths, but they also fail when the source is further from the array than the *equipartition distance*. This is the range scale over which the energy of the wave becomes distributed uniformly over the modes, independent of the source excitation. The waves scatter so much while they travel this distance that they lose all information of their initial state, thus making imaging impossible.

We show that in waveguides with interior inhomogeneities the equipartition distance is much longer than the scattering mean free path of the modes, so there is an observable range interval over which coherent imaging fails, but incoherent imaging succeeds. This is not the case for waveguides with perturbed boundaries where the equipartition distance is almost the same as the scattering mean free path of the fast modes. When coherent imaging fails in such waveguides, no imaging method can succeed, so there is no advantage in using the more complex, incoherent approaches.

The adaptive coherent imaging method proposed in this paper is based on a figure of merit of the quality of the image, which accounts for the trade-off between its statistical stability and resolution. There are many such figures of merit. We choose one that is simple and serves our purpose. In practice, it may be improved for example by incorporating prior information about the support of the source distribution. The method searches for weights of the data decomposed over the waveguide modes, in order to optimize the figure of merit. We apply the results of the asymptotic stochastic analysis in [8, 5, 6, 1] to derive theoretically the weights, and show that they are in good agreement with those from the numerical simulations in waveguides with random boundaries. We also show that coherent imaging fails in random waveguides with interior inhomogeneities, as predicted by the theory.

The paper is organized as follows. We begin in section 2 with the formulation of the problem. Then we describe in section 3 the model of the array data in ideal and randomly perturbed waveguides. The comparison of long range cumulative scattering effects of boundary perturbations and interior inhomogeneities is in section 4. The results motivate the adaptive coherent imaging method described and analyzed in section 5. The numerical simulations are in section 6. We end with a summary in section 7.

We dedicate this work to George Papanicolaou on the occasion of his 70th birthday.

2. Formulation of the source imaging problem. Consider a two-dimensional waveguide with range axis denoted by $z \in \mathbb{R}$ and transverse coordinate (cross-range) x belonging to a bounded interval, the waveguide cross-section, as illustrated in Figure 1.1. We assume a pressure release top boundary that may be perturbed, and a flat and rigid bottom boundary. Waveguides with perturbations of both boundaries are studied in [1].

The pressure field $p(t, x, z)$ satisfies the wave equation

$$\left[\partial_z^2 + \partial_x^2 - \frac{1}{c^2(x, z)} \partial_t^2 \right] p(t, x, z) = F(t, x, z), \quad x \in (0, \mathfrak{D}(z)), \quad z \in \mathbb{R}, \quad t > 0, \quad (2.1)$$

with boundary conditions

$$p(t, \mathfrak{D}(z), z) = \partial_x p(t, 0, z) = 0, \quad z \in \mathbb{R}, \quad t > 0. \quad (2.2)$$

Here t is time, $c(x, z)$ is the wave speed, $\mathfrak{D}(z)$ is the waveguide cross-section, and $F(t, x, z)$ models the source excitation. In ideal waveguides the boundaries are straight

$$\mathfrak{D}(z) = D, \quad \forall z \in \mathbb{R}, \quad (2.3)$$

and the wave speed is independent of range. We take it equal to the constant c_o . This simplification leads to explicit formulas in the analysis of coherent imaging, but the results extend to speeds that vary smoothly in x . In perturbed waveguides the boundary and the wave speed have small amplitude fluctuations

$$|\mathfrak{D}(z) - D| \ll D \quad \text{and} \quad |c(x, z) - c_o| \ll c_o, \quad (2.4)$$

modeled by random processes, as explained in sections 3.2 and 3.3.

We study the point spread function of coherent imaging methods, so we let

$$F(t, x, z) = e^{-i\omega_o t} f(Bt) \delta(x - x_o) \delta(z), \quad (2.5)$$

with the origin of the range axis at the point-like source, with cross-range coordinate x_o . The emitted signal is a pulse, modeled by function f of dimensionless arguments, with Fourier transform \hat{f} supported in the interval $[-\pi, \pi]$. The multiplication by the carrier oscillatory signal $e^{-i\omega_o t}$ centers the support of the Fourier transform of the pulse at ω_o ,

$$\int_{-\infty}^{\infty} dt e^{-i\omega_o t} f(Bt) e^{i\omega t} = \frac{1}{B} \hat{f} \left(\frac{\omega - \omega_o}{B} \right). \quad (2.6)$$

Therefore, the angular frequency ω , the dual variable to t , belongs to the interval $[\omega_o - \pi B, \omega_o + \pi B]$, where $\omega_o/(2\pi)$ is the central frequency, and B is the bandwidth.

The array is a collection of sensors that are far away from the source, at range z_A , and record the pressure field p . The recordings are the array data. The goal of coherent imaging is to superpose the data after proper synchronization and weighting, in order to form an imaging function. The synchronization is relative to a search point that sweeps a search domain where we seek the source. It amounts to solving backward the wave equation in the ideal waveguide, with the source at the array and the emitted signal given by the time reversed data. The imaging function is defined point-wise by the resulting solution at the search point. This process is called back-propagation.

A useful imaging function has the following qualities: (1) It peaks near the unknown source. (2) It is negligible away from the source. The smaller the domain

where it is large, the better the resolution. (3) It is robust with respect to the unknown perturbations in the waveguide.

Coherent imaging can succeed in random waveguides up to ranges where the array data maintain some coherence. The asymptotic stochastic theory developed in [8, 5, 6, 1] allows us to quantify the loss of coherence of the amplitudes of the waveguide modes. We use the results to explain the limitations of coherent imaging, and to motivate and analyze the adaptive imaging approach.

3. Model of the array data. We begin in section 3.1 with the model of the data in ideal waveguides. Then, we consider waveguides with a random pressure release boundary in section 3.2, and with random wave speed in section 3.3. The results extend to waveguides with both types of random perturbations. We separate them in order to compare their cumulative scattering effects on the imaging process.

3.1. Ideal waveguides. When the boundaries are flat and the wave speed is constant, the wave equation is separable and we can write the solution as a superposition of independent waveguide modes. A waveguide mode is a monochromatic wave $P(t, x, z) = \hat{P}(\omega, x, z)e^{-i\omega t}$, where $\hat{P}(\omega, x, z)$ satisfies the Helmholtz equation

$$[\partial_z^2 + \partial_x^2 + k^2] \hat{P}(\omega, x, z) = 0, \quad x \in (0, D), \quad z \in \mathbb{R}, \quad (3.1)$$

with boundary conditions

$$\hat{P}(\omega, D, z) = \partial_x \hat{P}(\omega, 0, z) = 0, \quad z \in \mathbb{R}, \quad (3.2)$$

and radiation conditions as $|z| \rightarrow \infty$. Here $k = \omega/c_o$ is the wavenumber.

The linear operator $\partial_x^2 + k^2$ defined on the vector space of functions in $C^2(0, D)$ that vanish at $x = D$ and have zero derivative at $x = 0$, is self-adjoint in $L_2(0, D)$. Its spectrum consists of a countable set of real and simple eigenvalues $\{\lambda_j(\omega)\}_{j \geq 1}$, assumed sorted in descending order. Because we assumed that c_o is constant, we can write them explicitly,

$$\lambda_j(\omega) = k^2 - \left[\frac{\pi(j-1/2)}{D} \right]^2, \quad j = 1, 2, \dots \quad (3.3)$$

The eigenfunctions form a complete orthonormal set in $L_2(0, D)$, and are given by

$$\phi_j(x) = \sqrt{\frac{2}{D}} \cos \left[\frac{\pi(j-1/2)x}{D} \right], \quad j = 1, 2, \dots \quad (3.4)$$

Note that only the first $N(\omega)$ eigenvalues are positive, where

$$N(\omega) = \lfloor kD/\pi + 1/2 \rfloor, \quad (3.5)$$

and $\lfloor \cdot \rfloor$ denotes the integer part. They define the modal wavenumbers $\beta_j(\omega) = \sqrt{\lambda_j(\omega)}$ of the forward (+) and backward (-) propagating modes

$$\hat{P}_j^{(\pm)}(\omega, x, z) = \phi_j(x) e^{\pm i\beta_j(\omega)z}, \quad j = 1, \dots, N(\omega). \quad (3.6)$$

The remaining infinitely many modes are evanescent

$$\hat{P}_j(\omega, x, z) = \phi_j(x) e^{-\beta_j(\omega)|z|}, \quad j > N(\omega), \quad (3.7)$$

with wavenumber $\beta_j(\omega) = \sqrt{-\lambda_j(\omega)}$.

3.1.1. Plane wave analogy. With the expression (3.4) of the eigenfunctions, we can write the forward propagating modes as

$$\widehat{P}_j^{(+)}(\omega, x, z) = \frac{1}{\sqrt{2D}} \left[e^{i\left(\frac{\pi(j-1/2)}{D}, \beta_j\right) \cdot (x, z)} + e^{i\left(-\frac{\pi(j-1/2)}{D}, \beta_j\right) \cdot (x, z)} \right]. \quad (3.8)$$

A similar formula holds for the backward propagating modes, with a negative sign in front of β_j . Equation (3.8) shows that the modes are associated with monochromatic plane waves that travel in the direction of the slowness vectors

$$\mathbf{K}_j = \left(\pm \frac{\pi(j-1/2)}{D}, \beta_j \right),$$

and strike the boundaries where they reflect. The slowness vectors of the first modes are almost parallel to the range axis,

$$\mathbf{K}_1 = \left(\pm \frac{\pi}{2D}, \beta_1 \right), \quad \frac{\pi}{2D} \approx \frac{k}{2N} \ll \beta_1 \approx k,$$

where the approximation is for a large $N(\omega)$. These waves travel quickly to the array, at speed that is approximately equal to c_o . The slowness vectors of the last modes are almost parallel to the x axis

$$\mathbf{K}_N = \left(\pm \frac{\pi(N-1/2)}{D}, \beta_N \right), \quad \frac{\pi(N-1/2)}{D} \approx k \gg \beta_N.$$

These waves strike the boundary many times, at almost normal incidence. They propagate very slowly to the array, on a long trajectory.

3.1.2. Data model. To simplify the analysis, we assume that the bandwidth is not too large, so that

$$N(\omega) = N(\omega_o), \quad \forall \omega \in [\omega_o - \pi B, \omega_o + \pi B]. \quad (3.9)$$

We denote henceforth the number of propagating modes by N , without any arguments. We also suppose that there are no standing waves in the waveguide, which means that none of the wavenumbers β_j vanish.

The pressure field for $z > 0$ is modeled by a superposition of forward going and evanescent waves

$$p(t, x, z) = \int \frac{d\omega}{2\pi} e^{-i\omega t} \left[\sum_{j=1}^N \frac{\widehat{a}_{j,o}(\omega)}{\sqrt{\beta_j(\omega)}} e^{i\beta_j(\omega)z} \phi_j(x) + \sum_{j=N+1}^{\infty} \frac{\widehat{e}_{j,o}(\omega)}{\sqrt{\beta_j(\omega)}} e^{-\beta_j(\omega)z} \phi_j(x) \right].$$

The modes do not interact with each other, so their amplitudes are independent of range. They are obtained from the source conditions

$$\begin{aligned} \widehat{p}(\omega, x, 0+) &= \widehat{p}(\omega, x, 0-), \\ \partial_z \widehat{p}(\omega, x, 0+) - \partial_z \widehat{p}(\omega, x, 0-) &= \frac{1}{B} \widehat{f} \left(\frac{\omega - \omega_o}{B} \right) \delta(x - x_o), \end{aligned}$$

which give

$$\begin{aligned} \widehat{a}_{j,o}(\omega) &= \frac{\phi_j(x_o)}{2iB\sqrt{\beta_j(\omega)}} \widehat{f} \left(\frac{\omega - \omega_o}{B} \right), \quad j = 1, \dots, N, \\ \widehat{e}_{j,o}(\omega) &= -\frac{\phi_j(x_o)}{2B\sqrt{\beta_j(\omega)}} \widehat{f} \left(\frac{\omega - \omega_o}{B} \right), \quad j > N. \end{aligned} \quad (3.10)$$

The model of the array data is given by

$$p(t, x, z_{\mathcal{A}}) \approx \sum_{j=1}^N \int \frac{d\omega}{2\pi B} \hat{f}\left(\frac{\omega - \omega_o}{B}\right) \frac{\phi_j(x_o)}{2i\beta_j(\omega)} \phi_j(x) e^{i\beta_j(\omega)z - i\omega t}. \quad (3.11)$$

The approximation is because we neglect the evanescent modes at the large range $z_{\mathcal{A}}$ of the array.

3.2. Waveguides with randomly perturbed boundary. The pressure release boundary has small fluctuations around the value D

$$\mathfrak{D}(z) = D \left[1 + \nu \left(\frac{z}{\ell} \right) \right], \quad (3.12)$$

where ν is a zero mean random process of dimensionless arguments. We assume that it is stationary and mixing, which means in particular that its covariance function

$$\mathcal{R}_{\nu}(\zeta) = \mathbb{E}[\nu(0)\nu(\zeta)] \quad (3.13)$$

is integrable over the real line. The scaling of the argument of ν in (3.12) indicates that the fluctuations are on the length scale ℓ , the correlation length.

Let ε be the small parameter that scales the amplitude of the fluctuations ν , defined by

$$\mathcal{R}_{\nu}(0) = \varepsilon^2 \ll 1. \quad (3.14)$$

The asymptotic analysis in [1] is with respect to ε , in the scaling regime

$$\ell \sim \lambda_o, \quad (3.15)$$

where λ_o is the reference, order one length scale. In this regime the waves interact efficiently with the random perturbations, but because their amplitude is small, their cumulative scattering effect is observable only at long ranges. It is shown in [1] that the scaling for studying the transition from coherent to incoherent waves should be

$$\varepsilon^2 z_{\mathcal{A}} \sim \lambda_o. \quad (3.16)$$

We recall directly from [1] the model of the pressure field

$$p(t, x, z_{\mathcal{A}}) \approx \int \frac{d\omega}{2\pi} \sum_{j=1}^N \frac{\hat{a}_j(\omega, z_{\mathcal{A}})}{\sqrt{\beta_j(\omega)}} \phi_j(x) e^{i\beta_j(\omega)z_{\mathcal{A}} - i\omega t}. \quad (3.17)$$

It is similar to equation (3.11), except that the mode amplitudes are random functions of frequency and range $z_{\mathcal{A}}$. They are analyzed in detail in [1]. Here we need only their first and second moments:

The mean mode amplitudes are

$$\mathbb{E}[\hat{a}_j(\omega, z_{\mathcal{A}})] \approx \frac{\phi_j(x_o)}{2iB\sqrt{\beta_j(\omega)}} \hat{f}\left(\frac{\omega - \omega_o}{B}\right) \exp\left[-\frac{z_{\mathcal{A}}}{\mathcal{S}_j(\omega)} + i\frac{z_{\mathcal{A}}}{\mathcal{L}_j(\omega)}\right], \quad (3.18)$$

where the approximation indicates that there is a vanishing residual in the limit $\varepsilon \rightarrow 0$. We recognize the first factor in (3.18) as $\hat{a}_{j,o}$, the j -th mode amplitude in

ideal waveguides. However, $\mathbb{E}[\hat{a}_j(\omega, z_A)]$ decays exponentially with z_A , on the length scale $\mathcal{S}_j(\omega)$ called the *scattering mean free path* of the j -th mode. It is given by

$$\frac{1}{\mathcal{S}_j(\omega)} = \frac{\pi^4 \ell (j-1/2)^2}{D^4 \beta_j(\omega)} \sum_{l=1}^N \frac{(l-1/2)^2}{\beta_l(\omega)} \widehat{\mathcal{R}}_\nu [(\beta_j(\omega) - \beta_l(\omega))\ell], \quad (3.19)$$

in terms of the power spectral density $\widehat{\mathcal{R}}_\nu$, the Fourier transform of the covariance \mathcal{R}_ν . We know that $\widehat{\mathcal{R}}_\nu \geq 0$ by Bochner's theorem, so all the terms in the sum are nonnegative.

Aside from the exponential decay, the mean amplitudes also display a net phase that increases with z_A on the mode-dependent length scales $\mathcal{L}_j(\omega)$. We recall¹ its expression from [1]

$$\begin{aligned} \frac{1}{\mathcal{L}_j(\omega)} &= \frac{\pi^4 \ell (j-1/2)^2}{D^4 \beta_j(\omega)} \mathcal{R}_\nu(0) \sum_{l=1}^N \frac{(l-1/2)^2}{\beta_l(\omega)} \gamma[\beta_j(\omega) - \beta_l(\omega)] \\ &+ \frac{\pi^2 (j-1/2)^2}{D^2 \beta_j(\omega)} \mathcal{R}_\nu(0) \left\{ -\frac{3}{2} + \sum_{l \neq j, l=1}^N \frac{[\beta_l(\omega) + \beta_j(\omega)] (l-1/2)^2}{\beta_l(\omega)(j+l-1)(j-l)} \right\} \\ &+ \frac{\mathcal{R}_\nu''(0)(j-1/2)^2}{\ell^2 \beta_j(\omega)} \left\{ \frac{\pi^2}{6} + \sum_{l \neq j, l=1}^N \frac{[\beta_j(\omega) - \beta_l(\omega)] (l-1/2)^2}{\beta_l(\omega)(j+l-1)^2(j-l)^2} \right\} + \kappa_j^{(e)}(\omega), \end{aligned}$$

where

$$\gamma(\beta) = 2 \int_0^\infty du \sin(\beta \ell u) \mathcal{R}_\nu(u),$$

and $\kappa_j^{(e)}(\omega)$ is due to the interaction of the evanescent waves with the propagating ones. It is given by

$$\begin{aligned} \kappa_j^{(e)}(\omega) &= \frac{2\pi^4 (j-1/2)^2}{D^4 \beta_j(\omega)} \sum_{l=N+1}^\infty \left\{ \frac{\ell (l-1/2)^2}{\beta_l(\omega)} \int_0^\infty du e^{-\ell \beta_l(\omega) u} \mathcal{R}_\nu(u) \cos[\ell \beta_j(\omega) u] \right. \\ &\left. - \frac{(l-1/2)^2}{\beta_j^2(\omega) + \beta_l^2(\omega)} \right\} - \frac{2 \mathcal{R}_\nu''(0) (j-1/2)^2}{\ell^2 \beta_j(\omega)} \sum_{l=N+1}^\infty \frac{(l-1/2)^2}{(l-j)^2(l+j-1)^2}, \end{aligned}$$

where we used integration by parts to simplify the formulas derived in [1].

The mean square mode amplitudes are

$$\mathbb{E} [|\hat{a}_j(\omega, z_A)|^2] \approx \frac{1}{4B^2} \left| \hat{f} \left(\frac{\omega - \omega_o}{B} \right) \right|^2 \sum_{l=1}^N \frac{\phi_l^2(x_o)}{\beta_l(\omega)} T_{jl}(\omega, z_A), \quad (3.20)$$

with $N \times N$ matrix

$$\mathbf{T}(\omega, z_A) = e^{\mathbf{\Gamma}^{(c)}(\omega) z_A},$$

¹Note that there is a typo in [1, Eq. (4.20)]: there is no minus sign in the definition of $\Gamma_{jj}^{(s)}(\omega)$

and symmetric $N \times N$ matrix $\mathbf{\Gamma}^{(c)}(\omega)$ defined by

$$\begin{aligned}\Gamma_{jl}^{(c)}(\omega) &= \frac{\pi^4 \ell (j - 1/2)^2 (l - 1/2)^2}{D^4 \beta_j(\omega) \beta_l(\omega)} \widehat{\mathcal{R}}_\nu [\ell(\beta_j(\omega) - \beta_l(\omega))], \quad j \neq l, \\ \Gamma_{jj}^{(c)}(\omega) &= - \sum_{l \neq j, l=1}^N \Gamma_{jl}^{(c)}(\omega), \quad j = 1, \dots, N.\end{aligned}\tag{3.21}$$

Let $\Lambda_j(\omega)$ be the eigenvalues of $\mathbf{\Gamma}^{(c)}$, in descending order, and $\mathbf{u}_j(\omega)$ its orthonormal eigenvectors. We have from the conservation of energy that

$$\Lambda_j(\omega) \leq 0,$$

so the limit $z_{\mathcal{A}} \rightarrow \infty$ of the matrix exponential

$$\mathbf{T}(\omega, z_{\mathcal{A}}) = e^{\mathbf{\Gamma}^{(c)}(\omega) z_{\mathcal{A}}} = \sum_{j=1}^N e^{\Lambda_j(\omega) z_{\mathcal{A}}} \mathbf{u}_j(\omega) \mathbf{u}_j^T(\omega),$$

is determined by the null space of $\mathbf{\Gamma}^{(c)}(\omega)$. Under the assumption that the power spectral density $\widehat{\mathcal{R}}_\nu$ does not vanish for any of the arguments in (3.21), $\mathbf{\Gamma}^{(c)}(\omega)$ is a Perron-Frobenius matrix with simple largest eigenvalue $\Lambda_1(\omega) = 0$. The leading eigenvector is given by

$$\mathbf{u}_1 = \frac{1}{\sqrt{N}}(1, \dots, 1)^T,$$

and as $z_{\mathcal{A}}$ grows,

$$\sup_{j,l=1,\dots,N} \left| T_{jl}(\omega, z_{\mathcal{A}}) - \frac{1}{N} \right| \leq O\left(e^{-\Lambda_2(\omega) z_{\mathcal{A}}}\right).\tag{3.22}$$

Thus, the right handside in (3.20) converges to a constant

$$\sum_{l=1}^N \frac{\phi_l^2(x_o)}{\beta_l(\omega)} T_{jl}(\omega, z_{\mathcal{A}}) \xrightarrow{z_{\mathcal{A}} \rightarrow \infty} \frac{1}{N} \sum_{l=1}^N \frac{\phi_l^2(x_o)}{\beta_l(\omega)},\tag{3.23}$$

on the length scale

$$\mathcal{L}_{\text{equip}} = -1/\Lambda_2(\omega),$$

called the *equipartition distance*. It is the range scale over which the energy becomes uniformly distributed over the modes, independent of the source excitation.

Equations (3.18), (3.20) and (3.23) give that the SNR (signal to noise ratio) of the amplitude of the j -th mode satisfies

$$\text{SNR}[\widehat{a}_j(\omega, z_{\mathcal{A}})] = \frac{|\mathbb{E}[\widehat{a}_j(\omega, z_{\mathcal{A}})]|}{\sqrt{\mathbb{E}\left[|\widehat{a}_j(\omega, z_{\mathcal{A}}) - \mathbb{E}[\widehat{a}_j(\omega, z_{\mathcal{A}})]|^2\right]}} \sim \exp\left[-\frac{z_{\mathcal{A}}}{\mathcal{S}_j(\omega)}\right].\tag{3.24}$$

Therefore, the j -th mode loses coherence on the range scale $\mathcal{S}_j(\omega)$, the scattering mean free path. The scaling (3.14) of the amplitude of the fluctuations ν implies that

$$\mathcal{S}_j \sim \varepsilon^{-2} \lambda_o,$$

so the loss of coherence can be observed at ranges of the order $\varepsilon^{-2} \lambda_o$, as stated in (3.22).

3.3. Waveguides with random medium. The boundaries in these waveguides are straight, but the wave speed is perturbed as

$$\frac{1}{c^2(x, z)} = \frac{1}{c_o^2} \left[1 + \mu \left(\frac{x}{\ell}, \frac{z}{\ell} \right) \right]. \quad (3.25)$$

Here $\mu(x, z)$ is a mean zero, statistically homogeneous random process of dimensionless arguments, with integrable autocorrelation

$$\mathcal{R}_\mu(\xi, \zeta) = \mathbb{E} [\mu(0, 0)\mu(\xi, \zeta)]. \quad (3.26)$$

As in the previous section, we model the small amplitude of the fluctuations using the small dimensionless parameter ε defined by

$$\mathcal{R}_\mu(0, 0) = \varepsilon^2 \ll 1. \quad (3.27)$$

The scaling by the correlation length ℓ of both arguments of μ indicates that the fluctuations are isotropic. We assume like before that $\ell \sim \lambda_o$, and use the same long range scaling (3.16) to study the loss of coherence of the waves due to cumulative scattering in the random medium.

The model of the array data, the mean and intensity of the mode amplitudes look the same as (3.17), (3.18) and (3.20), but the scattering mean free paths $\mathcal{S}_j(\omega)$, the net phases $\mathcal{L}_j(\omega)$ and the matrix $\mathbf{\Gamma}^{(c)}(\omega)$ are different. We recall their expression from [5, Chapter 20].

The scattering mean free path of the j -th mode is given by

$$\frac{1}{\mathcal{S}_j(\omega)} = \frac{k^4 \ell}{8\beta_j(\omega)} \sum_{l=1}^N \frac{1}{\beta_l(\omega)} \widehat{\mathcal{R}}_{\mu_{jl}} [(\beta_j(\omega) - \beta_l(\omega)) \ell], \quad (3.28)$$

where $\widehat{\mathcal{R}}_{\mu_{jl}}$ is the power spectral density of the stationary process

$$\mu_{jl}(\zeta) = \int_0^D dx \phi_j(x) \phi_l(x) \mu \left(\frac{x}{\ell}, \zeta \right), \quad (3.29)$$

with autocorrelation

$$\mathcal{R}_{\mu_{jl}}(\zeta) = \mathbb{E} [\mu_{jl}(0)\mu_{jl}(\zeta)]. \quad (3.30)$$

The net phase of the j -th mode is

$$\frac{1}{\mathcal{L}_j(\omega)} = \frac{k^4 \ell}{8\beta_j(\omega)} \sum_{l=1}^N \frac{1}{\beta_l(\omega)} \gamma_{jl} [\beta_j(\omega) - \beta_l(\omega)] + \kappa_j^{(e)}(\omega), \quad (3.31)$$

where

$$\gamma_{jl}(\beta) = 2 \int_0^\infty du \sin(\beta \ell u) \mathcal{R}_{\mu_{jl}}(u), \quad (3.32)$$

and the last term is due to the interaction of the evanescent modes with the propagating ones

$$\kappa_{jl}^{(e)}(\omega) = \frac{k^4 \ell}{2\beta_j(\omega)} \sum_{l=N+1}^\infty \frac{1}{\beta_l(\omega)} \int_0^\infty du e^{-\beta_l(\omega)u} \mathcal{R}_{\mu_{jl}}(u) \cos[\ell\beta_j(\omega)u]. \quad (3.33)$$

The matrix $\mathbf{\Gamma}^{(c)}(\omega)$ is symmetric, with entries given by

$$\begin{aligned}\Gamma_{jl}^{(c)}(\omega) &= \frac{k^4 \ell}{8\beta_j(\omega)\beta_l(\omega)} \widehat{\mathcal{R}}_{\mu_{jl}} [(\beta_j(\omega) - \beta_l(\omega)) \ell], \quad j \neq l, \\ \Gamma_{jj}^{(c)}(\omega) &= - \sum_{l \neq j, l=1}^N \Gamma_{jl}^{(c)}(\omega), \quad j = 1, \dots, N.\end{aligned}\tag{3.34}$$

As before, we denote its eigenvalues by $\Lambda_j(\omega) \leq 0$, and its orthonormal eigenvectors by \mathbf{u}_j , for $j = 1, \dots, N$. Moreover, assuming that the power spectral density $\widehat{\mathcal{R}}_{\mu_{jl}}$ does not vanish at any of the arguments $(\beta_j - \beta_l)\ell$, we obtain from the Perron-Frobenius theorem that the null space of $\mathbf{\Gamma}^{(c)}(\omega)$ is one-dimensional and spanned by

$$\mathbf{u}_1 = \frac{1}{\sqrt{N}}(1, 1, \dots, 1)^T.$$

The long range limit of the matrix exponential is as in (3.22), and the equipartition distance is given by $-1/\Lambda_2(\omega)$, in terms of the largest non-zero eigenvalue of $\mathbf{\Gamma}^{(c)}(\omega)$.

4. Comparisson of cumulative scattering effects. It is not difficult to see by inspection of formulas (3.19) and (3.28) that the scattering mean free paths \mathcal{S}_j and the net phase range scales \mathcal{L}_j decrease monotonically with the mode index. To obtain a quantitative comparison of the net scattering effects of boundary and medium perturbations, we consider here and in the numerical simulations two examples of autocorrelations of the fluctuations $\nu(\zeta)$ and $\mu(\xi, \zeta)$. The conclusions drawn below extend qualitatively to all fluctuations, but obviously, the scales depend on the expressions of \mathcal{R}_ν and \mathcal{R}_μ , the depth of the waveguide and the correlation length relative to λ_o .

We take henceforth $D = 20\lambda_o$, so that $N = 40$. The autocorrelation of the boundary fluctuations is of the so-called Matérn-7/2 form

$$\mathcal{R}_\nu(\zeta) = \varepsilon^2 \left(1 + |\zeta| + \frac{6\zeta^2}{15} + \frac{|\zeta|^3}{15} \right) e^{-|\zeta|},\tag{4.1}$$

with power spectral density

$$\widehat{\mathcal{R}}_\nu(\beta\ell) = \frac{32\varepsilon^2}{5[1 + (\beta\ell)^2]^4}.\tag{4.2}$$

The correlation length is $\ell = \lambda_o/\sqrt{5}$, and the amplitude of the fluctuations is scaled by $\varepsilon = 0.013$. The characteristic scales \mathcal{S}_j , \mathcal{L}_j and the equipartition distance $\mathcal{L}_{\text{equip}}$ are plotted in Figure 4.1.

The medium fluctuations have the Gaussian autocorrelation

$$\mathcal{R}_\mu(\xi, \zeta) = \varepsilon^2 e^{-\frac{\xi^2 + \zeta^2}{2}},\tag{4.3}$$

with correlation length $\ell = \lambda_o$ and amplitude scaled by $\varepsilon = 0.04$. The characteristic scales \mathcal{S}_j , \mathcal{L}_j and the equipartition distance $\mathcal{L}_{\text{equip}}$ are plotted in Figure 4.2.

We see in Figure 4.1 that the fast modes (with small index) have much larger scattering mean free paths than the slow ones in the waveguides with perturbed boundaries. When the arrays is at range $z_A \sim 100\lambda_o$, roughly half of the mode amplitudes remain coherent, and we can expect imaging to succeed if we filter out the

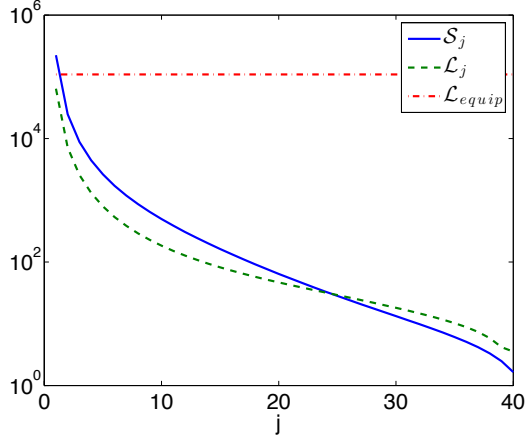


FIG. 4.1. The characteristic scales for a waveguide with random boundary. Here $D = 20\lambda_o$, $\ell = \lambda_o/\sqrt{5}$ and $\varepsilon = 0.013$. The abscissa is mode index and the ordinate is in units of λ_o .

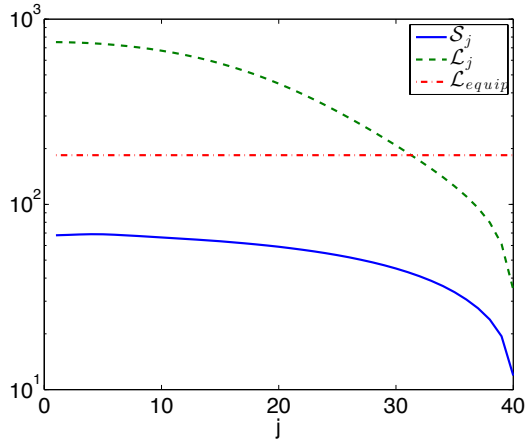


FIG. 4.2. The characteristic scales for a waveguide with random medium. Here $D = 20\lambda_o$, $\ell = \lambda_o$, and $\varepsilon = 0.04$. The abscissa is mode index and the ordinate is in units of λ_o .

slower modes, with index $j > 20$. As z_A increases, fewer and fewer modes remain coherent, and imaging should become more difficult. Once z_A exceeds the equipartition distance, which is similar to \mathcal{S}_1 in Figure 4.1, imaging becomes impossible, because the wave field forgets all the information about its initial state. Thus, when the wave field loses all its coherence, no imaging method can succeed in these waveguides.

Figure 4.2 shows that in media with random perturbations the scattering mean free paths of the fast modes are shorter, and that they decrease at a much slower rate with the mode index. No mode filtering can make coherent imaging succeed for $z_A \gtrsim 50\lambda_o \sim \mathcal{S}_1$, because all the mode amplitudes are incoherent. Since the equipartition distance is much larger than \mathcal{S}_1 , incoherent imaging is useful in these waveguides, in the range interval

$$50\lambda_o \sim \mathcal{S}_1 \lesssim z_A \leq \mathcal{L}_{\text{equip}} \sim 200\lambda_o.$$

5. Adaptive coherent imaging. We begin in section 5.1 with the formulation of the adaptive coherent imaging function. It models the backpropagation of the weighted time reversed data to search points in a fictitious ideal waveguide. The weights are chosen by optimizing a figure of merit of the image. We calculate them explicitly in ideal and random waveguides, in sections 5.2 and 5.3, respectively.

5.1. Coherent imaging. The data are collected at the array, with sensors located in the set $\{\mathbf{x}_r = (x_r, z_A), \quad r = 1, \dots, N_R\}$. The standard coherent imaging function is given by

$$\mathcal{I}(\mathbf{x}) = \int_{-\infty}^{\infty} \frac{d\omega}{2\pi} \frac{1}{N_R} \sum_{r=1}^{N_R} \overline{\widehat{p}(\omega, \mathbf{x}_r)} \widehat{G}_o(\omega, \mathbf{x}_r, \mathbf{x}), \quad (5.1)$$

where $\mathbf{x} = (x, z)$ are points in a search domain containing the unknown location $\mathbf{x}_o = (x_o, 0)$ of the source, and \widehat{G}_o is the outgoing Green's function in the ideal waveguide. It models the propagation from \mathbf{x}_r to \mathbf{x} , of the time reversed array data with Fourier transform $\widehat{p}(\omega, \mathbf{x}_r)$, where the bar denotes complex conjugation.

We see from (3.11) that

$$\widehat{G}_o(\omega, \mathbf{x}_r, \mathbf{x}) = \sum_{j=1}^N \frac{\phi_j(x_r)}{2i\beta_j(\omega)} \phi_j(x) e^{i\beta_j(\omega)(z_A - z)}, \quad (5.2)$$

so we can rewrite (5.1) as

$$\mathcal{I}(\mathbf{x}) = \int_{-\infty}^{\infty} \frac{d\omega}{2\pi} \sum_{j=1}^N \frac{1}{2i\beta_j(\omega)} \overline{\widehat{p}_j(\omega, z_A)} \phi_j(x) e^{i\beta_j(\omega)(z_A - z)} \quad (5.3)$$

with

$$\widehat{p}_j(\omega, z_A) = \frac{1}{N_R} \sum_{r=1}^{N_R} \widehat{p}(\omega, \mathbf{x}_r) \phi_j(x_r). \quad (5.4)$$

The adaptive coherent imaging function is a modification of (5.3)

$$\mathcal{I}(\mathbf{x}; \mathbf{w}) = \int_{-\infty}^{\infty} \frac{d\omega}{2\pi} \sum_{j=1}^N \frac{w_j}{2i\beta_j(\omega)} \overline{\widehat{p}_j(\omega, z_A)} \phi_j(x) e^{i\beta_j(\omega)(z_A - z)}, \quad (5.5)$$

with data components $\widehat{p}_j(\omega, z_A)$ weighted by the entries in the complex vector

$$\mathbf{w} = (w_1, \dots, w_N)^T \in \mathbb{C}^N,$$

with Euclidian norm

$$\|\mathbf{w}\| = \sqrt{\sum_{j=1}^N |w_j|^2} = 1. \quad (5.6)$$

5.1.1. Weight optimization. We wish to optimize the weights so as to maximize the ratio of the peak amplitude of the image normalized by its L^2 -norm,

$$\mathbf{w}^* = \operatorname{argmax}_{\mathbf{w} \in \mathbb{W}} \mathcal{M}(\mathbf{w}), \quad \mathcal{M}(\mathbf{w}) = \frac{|\mathcal{I}(\mathbf{x}^*; \mathbf{w})|^2}{\|\mathcal{I}(\cdot; \mathbf{w})\|^2}, \quad (5.7)$$

where

$$\mathbb{W} = \left\{ \mathbf{w} = (w_1, \dots, w_N)^T \in \mathbb{C}^N, \quad \sum_{j=1}^N |w_j|^2 = 1 \right\},$$

and

$$\|\mathcal{I}(\cdot; \mathbf{w})\|^2 = \int_0^D dx \int_{-\infty}^{\infty} dz |\mathcal{I}(\mathbf{x}; \mathbf{w})|^2.$$

The peak location \mathbf{x}^* is expected to be at \mathbf{x}_o , where the source lies, and the optimization intends to focus the image around it. This is certainly true in ideal waveguides. In random waveguides we need to ensure that the image is robust with respect to the unknown perturbations. If this is not so, the image will have spurious peaks.

There are two requirements for obtaining robust images: The first is that only the modes that are coherent contribute to the image. Thus, the weights should null the modes with scattering mean free paths that are shorter than the range of the array. The second is that the bandwidth be much larger than the decoherence frequency of the data. This ensures that the incoherent part of the data averages out when we integrate over the frequencies, like in the law of large numbers.

It is shown in [1] and [5, Chapter 20] that in our regime the decoherence frequency is very small, of the order $\varepsilon^2 \omega_o$. Therefore, it is possible to have a bandwidth that is small with respect to the central frequency, as assumed in section 3.1.2, and large with respect to the decoherence frequency.

As long as the two requirements above hold, we can analyze the optimal weights using the theoretical figure of merit

$$\mathcal{M}_{\text{th}}(\mathbf{w}) = \frac{|\mathbb{E} [\mathcal{I}(\mathbf{x}_o; \mathbf{w})]|^2}{\mathbb{E} [\|\mathcal{I}(\cdot; \mathbf{w})\|^2]}. \quad (5.8)$$

5.1.2. Simplifying assumptions. In the analysis we suppose that the recordings of the acoustic pressure are over an infinitely long time window, and approximate the array by a continuum aperture, so that in the imaging function we can replace sums over the sensors by integrals over the aperture. In particular, we have

$$\widehat{p}_j(\omega, z_A) = \frac{1}{N_R} \sum_{r=1}^{N_R} \widehat{p}(\omega, \mathbf{x}_r) \phi_j(x_r) \approx \int_0^D dx 1_{\mathcal{A}}(x) \widehat{p}(\omega, x, z_A) \phi_j(x), \quad (5.9)$$

where $1_{\mathcal{A}}$ is the indicator function of the array. It is equal to one in the cross-range support of the array and zero otherwise. The continuum approximation is valid when the sensors are close together, at less than half a central wavelength $\lambda_o = 2\pi c_o/\omega_o$ apart.

We consider a full aperture array, spanning the entire cross-section of the waveguide, so the indicator function $1_{\mathcal{A}}$ in (5.9) is identically one. The results extend to

partial apertures, but the formulas are more complicated and the optimal weights are not easy to interpret.

All these assumptions allow us to simplify the expression of the imaging function, so that we can focus attention on the cumulative scattering effects due to the random perturbations of the waveguide.

5.2. Coherent imaging in ideal waveguides. In this section we address the case in which the waveguide is ideal, i.e. without any random perturbation.

5.2.1. Determination of the optimal weights. We obtain from the model (3.11) of the array data and the orthogonality of the eigenfunctions that

$$\hat{p}_j(\omega) = \frac{1}{B} \hat{f}\left(\frac{\omega - \omega_o}{B}\right) \frac{\phi_j(x_o)}{2i\beta_j(\omega)} e^{i\beta_j(\omega)z_A}, \quad (5.10)$$

and therefore

$$\begin{aligned} \mathcal{I}(\mathbf{x}; \mathbf{w}) &= \frac{1}{4} \int_{-\infty}^{\infty} \frac{d\omega}{2\pi B} \overline{\hat{f}\left(\frac{\omega - \omega_o}{B}\right)} \sum_{j=1}^N \frac{w_j}{\beta_j^2(\omega)} \phi_j(x) \phi_j(x_o) e^{-i\beta_j(\omega)z} \\ &\approx \frac{1}{4} \sum_{j=1}^N \frac{w_j}{\beta_j^2(\omega_o)} \phi_j(x) \phi_j(x_o) \mathfrak{F}_j(z). \end{aligned} \quad (5.11)$$

Here we used that $B \ll \omega_o$ and introduced the mode pulses

$$\begin{aligned} \mathfrak{F}_j(z) &= \int_{-\infty}^{\infty} \frac{d\omega}{2\pi B} \overline{\hat{f}\left(\frac{\omega - \omega_o}{B}\right)} e^{-i\beta_j(\omega)z} \\ &= \int_{-\infty}^{\infty} \frac{dh}{2\pi} \overline{\hat{f}(h)} e^{-i\beta_j(\omega_o + Bh)z} \\ &\approx e^{-i\beta_j(\omega_o)z} f[-\beta'_j(\omega_o)Bz] \end{aligned} \quad (5.12)$$

that peak at the range $z = 0$ of the source, with mode- and bandwidth-dependent resolution. The modes propagate at speed

$$\frac{1}{\beta'_j(\omega_o)} = c_o \frac{\beta_j(\omega_o)}{k_o}, \quad (5.13)$$

where $k_o = 2\pi/\lambda_o$, and the range resolution of $\mathfrak{F}_j(z)$ is determined by the distance traveled at this speed over the duration $\sim 1/B$ of the pulse.

The focusing in cross-range is due to the summation over the modes. Explicitly, when we evaluate (5.11) at the range of the source, we obtain

$$\mathcal{I}((x, 0); \mathbf{w}) \approx \frac{f(0)}{4} \sum_{j=1}^N \frac{w_j}{\beta_j^2(\omega_o)} \phi_j(x) \phi_j(x_o). \quad (5.14)$$

This is a sum of oscillatory terms unless $x = x_o$, so the image peaks at $x = x_o$, with resolution depending on the weights.

The figure of merit (5.7) is the ratio of the peak intensity

$$|\mathcal{I}(\mathbf{x}_o; \mathbf{w})|^2 \approx \frac{|f(0)|^2}{16} \left| \sum_{j=1}^N \frac{w_j}{\beta_j^2(\omega_o)} \phi_j^2(x_o) \right|^2 \quad (5.15)$$

and the L_2 norm

$$\begin{aligned}
\|\mathcal{I}(\cdot; \mathbf{w})\|^2 &= \int_0^D dx \int_{-\infty}^{\infty} dz |\mathcal{I}(\mathbf{x}; \mathbf{w})|^2 \\
&\approx \sum_{j=1}^N \frac{|w_j|^2 \phi_j^2(x_o)}{16\beta_j^4(\omega_o)} \int_{-\infty}^{\infty} \frac{dh}{2\pi} \widehat{f}(h) \int_{-\infty}^{\infty} \frac{dh'}{2\pi} \widehat{f}(h') \int_{-\infty}^{\infty} dz e^{i[\beta_j(\omega_o+hB)-\beta_j(\omega_o+Bh')]z} \\
&= \frac{\|f\|^2 c_o^2}{16B\omega_o} \sum_{j=1}^N \frac{|w_j|^2}{\beta_j^3(\omega_o)} \phi_j^2(x_o). \tag{5.16}
\end{aligned}$$

Here we used the orthonormality of the eigenfunctions, and relation (5.13). We also introduced the notation

$$\|f\|^2 = \int_{-\infty}^{\infty} \frac{d\omega}{2\pi} |\widehat{f}(\omega)|^2 = \int_{-\infty}^{\infty} dt |f(t)|^2.$$

The figure of merit becomes

$$\mathcal{M}(\mathbf{w}) = C \frac{\left| \sum_{j=1}^N \frac{w_j}{\beta_j^2(\omega_o)} \phi_j^2(x_o) \right|^2}{\sum_{j=1}^N \frac{|w_j|^2}{\beta_j^3(\omega_o)} \phi_j^2(x_o)}, \tag{5.17}$$

with constant

$$C = \frac{B\omega_o |f(0)|^2}{c_o^2 \|f\|^2}$$

that plays no role in the optimization. Because \mathcal{M} is homogeneous of degree zero in \mathbf{w} , we can maximize $\mathcal{M}(\mathbf{w})$ to obtain the optimal \mathbf{w}^* up to a multiplicative constant that we can then determine from the normalization condition $\|\mathbf{w}^*\| = 1$. The result is

$$\begin{aligned}
w_j^* &= \frac{\beta_j(\omega_o)}{\|\beta\|_{x_o}}, \quad j \in \mathbb{J}_{x_o} = \{j = 1, \dots, N, \text{ s.t. } \phi_j(x_o) \neq 0\}, \tag{5.18} \\
w_j^* &= 0, \quad j \in \mathbb{J}_{x_o}^c = \{1, \dots, N\} \setminus \mathbb{J}_{x_o},
\end{aligned}$$

where we introduced the notation

$$\|\beta\|_{x_o} := \sqrt{\sum_{j \in \mathbb{J}_{x_o}} \beta_j^2(\omega_o)}.$$

When the set $\mathbb{J}_{x_o}^c$ is empty, there is a unique maximizer \mathbf{w}^* . Otherwise, there are infinitely many maximizers, with arbitrary weights for mode indexes $j \in \mathbb{J}_{x_o}^c$. Equations (5.18) define just one solution. Note however that all maxima of $\mathcal{M}(\mathbf{w})$ are global maxima, because the weights indexed by $j \in \mathbb{J}_{x_o}^c$ multiply $\phi_j(x_o) = 0$ in the figure of merit, and they play no role in the behavior of the imaging function, given by

$$\mathcal{I}(\mathbf{x}; \mathbf{w}^*) \approx \frac{1}{4\|\beta\|_{x_o}} \sum_{j \in \mathbb{J}_{x_o}} \frac{\phi_j(x) \phi_j(x_o)}{\beta_j(\omega_o)} e^{-i\beta_j(\omega_o)z} f[-\beta_j'(\omega_o)Bz]. \tag{5.19}$$

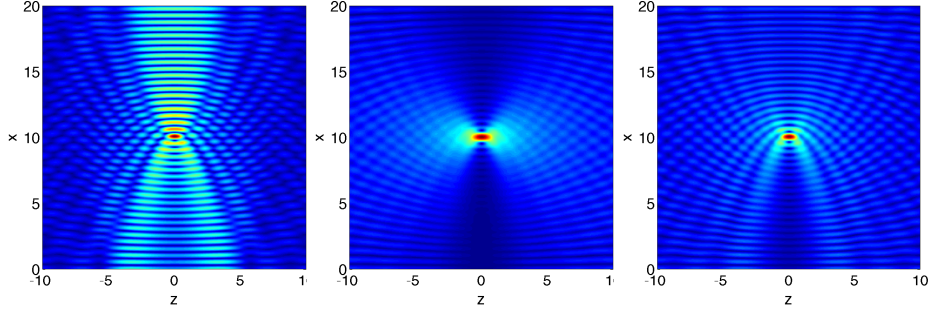


FIG. 5.1. The image $\mathcal{I}(\mathbf{x}; \mathbf{w})$ for weights $w_j = 1/\sqrt{N}$ (left), $\mathbf{w} = \mathbf{w}^{\text{cr}}$ (middle) and $\mathbf{w} = \mathbf{w}^*$ (right). The abscissa is the range z in λ_o and the ordinate the cross-range in λ_o . Here $D = 20\lambda_o$, and the pulse is defined in (5.20).

5.2.2. Discussion. To motivate the figure of merit (5.17) and illustrate the effect of the optimization on the image, let us set $x_o = D/2$ and consider a Gaussian pulse

$$f(u) = e^{-u^2/2} \quad (5.20)$$

with bandwidth $\pi B = 0.025\omega_o$.

We display the absolute value of the image $\mathcal{I}(\mathbf{x}; \mathbf{w}^*)$ in the right plot of Figure 5.1. For comparison, we show in the left plot of Figure 5.1 the image with the uniform weights $w_j = 1/\sqrt{N}$. It has prominent fringes in the cross-range, which are mitigated by the optimization over the weights. We do not get the best cross-range resolution with the weights (5.18). The optimal $\mathbf{w}^{\text{cr}} \in \mathbb{W}$ for focusing in cross-range has components

$$w_j^{\text{cr}} = \frac{\beta_j^2(\omega_o)}{\|\beta^2\|_{x_o}}, \quad j \in \mathbb{J}_{x_o}, \quad \|\beta^2\|_{x_o} = \sqrt{\sum_{j \in \mathbb{J}_{x_o}} \beta_j^4(\omega_o)}.$$

It maximizes the ratio of the peak of the image and its mean square along the cross-range line at $z = 0$,

$$\mathcal{M}^{\text{cr}}(\mathbf{w}) = \frac{|\mathcal{I}(\mathbf{x}_o; \mathbf{w})|^2}{\|\mathcal{I}(\cdot, 0); \mathbf{w}\|^2}, \quad \|\mathcal{I}(\cdot, 0); \mathbf{w}\|^2 = \int_0^D dx |\mathcal{I}((x, 0); \mathbf{w})|^2, \quad (5.21)$$

and gives the image

$$\mathcal{I}(\mathbf{x}; \mathbf{w}^{\text{cr}}) \approx \frac{1}{4\|\beta^2\|_{x_o}} \sum_{j \in \mathbb{J}_{x_o}} \phi_j(x) \phi_j(x_o) e^{-i\beta_j(\omega_o)z} f[-\beta_j'(\omega_o)Bz].$$

We show it in the middle plot of Figure 5.1, and indeed, it has smaller fringes along the axis $z = 0$. However, the range resolution is worse than that given by the optimal weights.

It is easy to see that the optimal $\mathbf{w}^{\text{r}} \in \mathbb{W}$ for focusing in range, the maximizer of

$$\mathcal{M}^{\text{r}}(\mathbf{w}) = \frac{|\mathcal{I}(\mathbf{x}_o; \mathbf{w})|^2}{\|\mathcal{I}((x_o, \cdot); \mathbf{w})\|^2}, \quad \|\mathcal{I}((x_o, \cdot); \mathbf{w})\|^2 = \int_{-\infty}^{\infty} dz |\mathcal{I}((x_o, z); \mathbf{w})|^2, \quad (5.22)$$

has the components

$$w_j^r = C^r \frac{\beta_j(\omega_o)}{\phi_j^2(x_o)}, \quad j \in \mathbb{J}_{x_o},$$

with constant

$$C^r = 1 / \sqrt{\sum_{l \in \mathbb{J}_{x_o}} \beta_l^2(\omega_o) / \phi_l^4(x_o)}.$$

When $x_o = D/2$ we have $\phi_j^2(x_o) = 1/D$ for all j , and therefore $\mathbf{w}^r = \mathbf{w}^*$. For all other x_o we have $\mathbf{w}^r \neq \mathbf{w}^*$, and the image is given by

$$\mathcal{I}(\mathbf{x}; \mathbf{w}^r) = \frac{C^r}{4} \sum_{j \in \mathbb{J}_{x_o}} \frac{e^{-i\beta_j(\omega_o)z}}{\beta_j(\omega_o)} f[-\beta_j^l(\omega_o)Bz]$$

Our optimization finds a compromise between cross-range and range focusing, which is achieved at the maximum of the figure of merit $\mathcal{M}(\mathbf{w})$. We can determine explicitly the cross-range and range resolution of $\mathcal{I}(\mathbf{x}; \mathbf{w}^*)$ under the assumption that $N \gg 1$ (that is, $D \gg \lambda_o$). Then, we can replace the sum over the modes by an integral over the variable $u = j/N \in (0, 1]$, and obtain from the expressions of ϕ_j and β_j that

$$\begin{aligned} \mathcal{I}((x, 0); \mathbf{w}^*) &\sim \int_0^1 du \frac{\cos[uk_o(x - x_o)]}{\sqrt{1 - u^2}} + \int_0^1 du \frac{\cos[uk_o(x + x_o)]}{\sqrt{1 - u^2}} \\ &= \frac{\pi}{2} J_0[k_o(x - x_o)] + \frac{\pi}{2} J_0[k_o(x + x_o)] \\ &\approx \frac{\pi}{2} J_0[k_o(x - x_o)], \end{aligned} \quad (5.23)$$

where J_0 is the Bessel function of the first kind of order zero, and \sim denotes approximate, up to a multiplicative constant. The cross-range resolution is estimated as the distance between the peak of J_0 that occurs at zero, and its first zero, that occurs at $k_o|x - x_o| \approx 2.4$. We obtain that

$$|x - x_o| \lesssim \frac{2.4\lambda_o}{2\pi} \sim \frac{\lambda_o}{2}, \quad (5.24)$$

which is basically the diffraction limit of half a wavelength.

For the focusing in range we have

$$\begin{aligned} \mathcal{I}((x_o, z); \mathbf{w}^*) &\sim \int_0^1 du \frac{e^{-ik_o z \sqrt{1 - u^2}}}{\sqrt{1 - u^2}} \exp\left[-\frac{(Bz)^2}{2c_o^2(1 - u^2)}\right] \\ &\approx \int_0^1 du \frac{e^{-ik_o z \sqrt{1 - u^2}}}{\sqrt{1 - u^2}} \\ &= \frac{\pi}{2} J_o(k_o z) - \frac{i\pi}{2} H_o(k_o z), \end{aligned} \quad (5.25)$$

where we used that $x_o = D/2$ and neglected the effect of the pulse because $B \ll \omega_o$. The result is in terms of the Bessel function J_o and the Struve function H_o , and it is plotted in Figure 5.2. The range resolution is of the order λ_o .

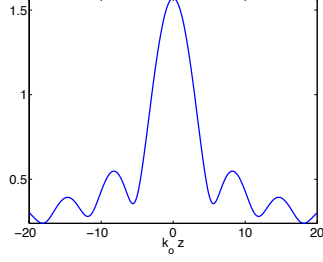


FIG. 5.2. The absolute value of the right hand side in (5.25), which describes the range resolution, as a function of $k_o z$.

5.3. Random waveguides. We use the figure of merit (5.8) to analyze the optimal weights for imaging in random waveguides. This is justified as long as the imaging process remains statistically stable, as explained in section 5.1.1. When the data become incoherent, that is when the array is farther than the scattering mean free path of all the modes, the weights predicted by the analysis are not useful. The images have spurious peaks that change unpredictably with the realization of the random waveguides (the random fluctuations of \mathcal{I} dominate the mean $\mathbb{E}[\mathcal{I}]$). We cannot use coherent imaging for such data no matter how we weight its components.

5.3.1. The first two moments of the imaging function. The imaging function follows from equations (3.17), (5.3) and (5.9), for the full aperture array

$$\mathcal{I}(\mathbf{x}; \mathbf{w}) \approx \sum_{j=1}^N \int_{-\infty}^{\infty} \frac{d\omega}{2\pi} \sum_{j=1}^N \frac{w_j \overline{\widehat{a}_j(\omega, z_A)}}{2i\beta_j^{3/2}(\omega)} \phi_j(x) e^{-i\beta_j(\omega)z}. \quad (5.26)$$

We compute its mean and intensity using the moment formulas (3.18) and (3.20). We have

$$\mathbb{E}[\mathcal{I}(\mathbf{x}; \mathbf{w})] \approx \frac{1}{4} \sum_{j=1}^N \frac{w_j}{\beta_j^2(\omega_o)} \phi_j(x) \phi_j(x_o) \mathfrak{F}_j(z) \exp\left[-\frac{z_A}{\mathcal{S}_j(\omega_o)} - i\frac{z_A}{\mathcal{L}_j(\omega_o)}\right], \quad (5.27)$$

with mode pulses $\mathfrak{F}_j(z)$ defined in (5.12). This expression is similar to that of the imaging function in ideal waveguides given by (5.11), except that the contribution of the j -th mode is damped on the range scale \mathcal{S}_j and is modulated by oscillation on the range scale \mathcal{L}_j . This oscillation must be removed in order to focus the image, which is why we should allow the weights w_j to be complex.

The intensity of the image is

$$\begin{aligned} \mathbb{E}[|\mathcal{I}(\mathbf{x}; \mathbf{w})|^2] &\approx \frac{1}{4} \sum_{j,j'=1}^N \frac{w_j \overline{w_{j'}}}{\beta_j^{3/2}(\omega_o) \beta_{j'}^{3/2}(\omega_o)} \int_{-\infty}^{\infty} \frac{d\omega}{2\pi} \int_{-\infty}^{\infty} \frac{d\omega'}{2\pi} \mathbb{E}[\overline{\widehat{a}_j(\omega, z_A)} \widehat{a}_{j'}(\omega', z_A)] \\ &\quad \times \phi_j(x) \phi_{j'}(x) e^{i[\beta_{j'}(\omega') - \beta_j(\omega)]z} \end{aligned} \quad (5.28)$$

and its square L^2 norm is given by

$$\begin{aligned}\mathbb{E} \left[\|\mathcal{I}(\cdot; \mathbf{w})\|^2 \right] &= \int_0^D dx \int_{-\infty}^{\infty} dz \mathbb{E} \left[|\mathcal{I}(\mathbf{x}; \mathbf{w})|^2 \right] \\ &= \frac{1}{4} \sum_{j=1}^N \frac{|w_j|^2}{\beta_j^3(\omega_o)} \int_{-\infty}^{\infty} \frac{d\omega}{2\pi} \int_{-\infty}^{\infty} \frac{d\omega'}{2\pi} \mathbb{E} \left[\overline{\widehat{a}_j(\omega, z_{\mathcal{A}})} \widehat{a}_j(\omega', z_{\mathcal{A}}) \right] \int_{-\infty}^{\infty} dz e^{i[\beta_j(\omega') - \beta_j(\omega)]z} \\ &\approx \frac{1}{4} \sum_{j=1}^N \frac{|w_j|^2}{\beta_j^3(\omega_o) \beta'_j(\omega_o)} \int_{-\infty}^{\infty} \frac{d\omega}{2\pi} \mathbb{E} \left[|\widehat{a}_j(\omega, z_{\mathcal{A}})|^2 \right],\end{aligned}$$

because of the orthonormality of the eigenfunctions $\phi_j(x)$. Recalling the moment formula (3.20) and using equation (5.13), we obtain

$$\mathbb{E} \left[\|\mathcal{I}(\cdot; \mathbf{w})\|^2 \right] \approx \frac{c_o \|f\|^2}{16k_o B} \sum_{j=1}^N \frac{|w_j|^2}{\beta_j^2(\omega_o)} \sum_{l=1}^N \frac{\phi_l^2(x_o) T_{jl}(\omega_o, z_{\mathcal{A}})}{\beta_l(\omega_o)}. \quad (5.29)$$

5.3.2. Optimal weights. The weights must compensate for the oscillations in (5.27) in order for $\mathbb{E} [\mathcal{I}(\mathbf{x}; \mathbf{w})]$ to peak at the source location \mathbf{x}_o . Thus, we let

$$w_j = w_j^+ \exp \left[i \frac{z_{\mathcal{A}}}{\mathcal{L}_j(\omega_o)} \right], \quad w_j^+ = |w_j|, \quad (5.30)$$

and maximize

$$\mathcal{M}_{\text{th}}(\mathbf{w}^+) = \frac{\mathbb{E} [\|\mathcal{I}(\mathbf{x}_o; \mathbf{w})\|^2]}{\mathbb{E} [\|\mathcal{I}(\cdot; \mathbf{w})\|^2]} \sim \frac{\left[\sum_{j=1}^N \frac{w_j^+ \phi_j^2(x_o)}{\beta_j^2(\omega_o)} \exp \left(-\frac{z_{\mathcal{A}}}{\mathcal{S}_j(\omega_o)} \right) \right]^2}{\sum_{j=1}^N \frac{(w_j^+)^2}{\beta_j^2(\omega_o)} \sum_{l=1}^N \frac{\phi_l^2(x_o) T_{jl}(\omega_o, z_{\mathcal{A}})}{\beta_l(\omega_o)}}, \quad (5.31)$$

over the vectors $\mathbf{w}^+ = (w_1^+, \dots, w_N^+)^T$ with non-negative entries, and Euclidian norm $\|\mathbf{w}^+\| = 1$. The symbol \sim denotes approximate, up to a multiplicative constant, as before.

The optimal weights are given by

$$w_j^+ = \frac{C \phi_j^2(x_o) \exp \left(-\frac{z_{\mathcal{A}}}{\mathcal{S}_j(\omega_o)} \right)}{\sum_{l=1}^N \frac{\phi_l^2(x_o) T_{jl}(\omega_o, z_{\mathcal{A}})}{\beta_l(\omega_o)}}, \quad j \in \mathbb{J}_{x_o}, \quad (5.32)$$

with positive constant C determined by the normalization $\|\mathbf{w}^+\| = 1$. They are damped exponentially with range on the scale given by the mode dependent scattering mean free paths \mathcal{S}_j . The optimization detects the modes that are incoherent, i.e., the indexes j for which $z_{\mathcal{A}} > \mathcal{S}_j(\omega_o)$, and suppresses them in the data.

6. Numerical simulations. In this section we present numerical simulations and compare the results with those predicted by the theory. The setup is as described in section 4, with autocorrelation functions (4.1) and (4.3) of the perturbations of the boundary and of the wave speed, in a waveguide of depth $D = 20\lambda_o$. All lengths

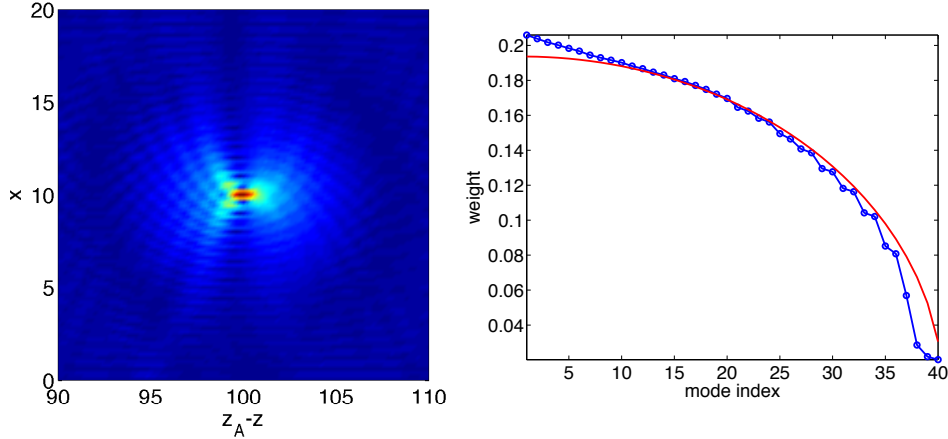


FIG. 6.1. Homogeneous medium and array range $z_A = 100\lambda_o$. Left: Image with the numerically computed weights. The abscissa is $z_A - z$ in λ_o and the ordinate is the cross-range x in λ_o . Right: Theoretical weights (in red) and numerical ones (in blue) vs. mode index.

are scaled by the central wavelength λ_o , and the bandwidth satisfies $\pi B = 0.0625\omega_o$. For example, we could have the central frequency 1kHz and the unperturbed wave speed $c_o = 1\text{km/s}$, so that $\lambda_o = 1\text{m}$ and $B = 0.125\text{kHz}$. To illustrate the cumulative scattering effect on the imaging process, we consider several ranges z_A of the array, from $25\lambda_o$ to $150\lambda_o$. The details on the numerical simulations of the array data are in appendix A

We begin in Figure 6.1 with the results in an ideal waveguide, with array at range $z_A = 100\lambda_o$. We plot on the left the image with the optimal weights and on the right the theoretical weights (5.18) (in red) and the numerically computed weights (in blue). The weights are computed by minimizing $1/\mathcal{M}(\mathbf{w})$, with \mathcal{M} defined in (5.7). The optimization is done with the MATLAB function *fmincon*, over weights $\mathbf{w} = (w_1, \dots, w_N)^T \in \mathbb{R}^N$, with constraints $w_j \geq 0$ for $j = 1, \dots, N$, and normalization $\|\mathbf{w}\|^2 = 1$. The image is very similar to that predicted by the theory (the right plot in Figure 5.1), and the optimal weights are in agreement, as well.

The analysis for random waveguides in section 5.3 is based on the theoretical figure of merit (5.8), which is close to $\mathcal{M}(\mathbf{w})$ only when the image is statistically stable. The theory in [1, 8, 5] predicts that stability holds for the given bandwidth, in the asymptotic limit $\varepsilon \rightarrow 0$. We have a finite ε , and to stabilize the optimization so that we can compare it with the theory, we need to work with a slight modification of the figure of merit (5.7),

$$\mathcal{M}_{\text{num}}(\mathbf{w}) = \frac{|\langle \mathcal{I}(\mathbf{x}_o; \mathbf{w}) \rangle|^2}{\|\mathcal{I}(\cdot; \mathbf{w})\|^2}, \quad (6.1)$$

where $\langle \mathcal{I}(\mathbf{x}_o; \mathbf{w}) \rangle$ is a local spatial average of the image around \mathbf{x}_o .

In our regime the theory predicts that $\mathcal{L}_j > z_A$ for all the modes that remain coherent, as shown in Figures 4.1 and 4.2. Therefore, we can neglect the phase factors in (5.30), and optimize directly over positive weights. The optimization is done with the MATLAB function *fmincon*, as before, but we regularize it by asking that the weights be monotone decreasing with the mode index. That is to say, we work with

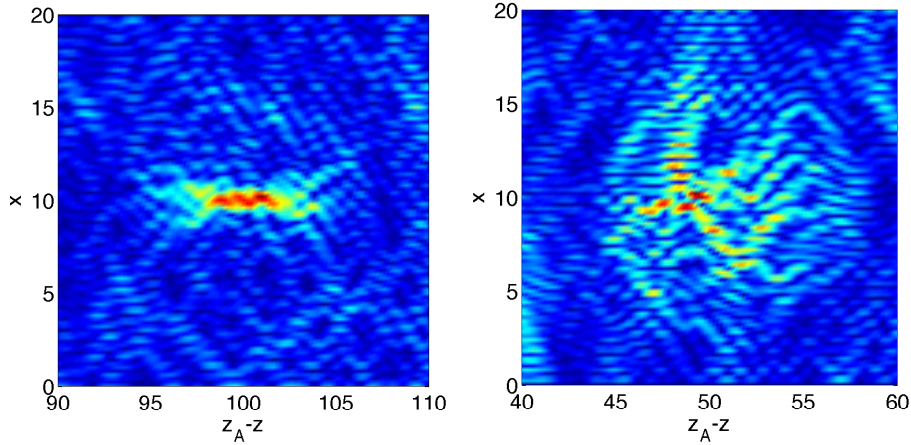


FIG. 6.2. Image $\mathcal{I}(\mathbf{x}; \mathbf{w})$ in waveguide with perturbed boundary and array at range $z_{\mathcal{A}} = 100\lambda_o$ (left) and in waveguide with perturbed medium and array at range $z_{\mathcal{A}} = 50\lambda_o$ (right). The weights are uniform $w_j = 1/\sqrt{N}$, for $j = 1, \dots, N$. The abscissa is $z_{\mathcal{A}} - z$ in λ_o and the ordinate is the cross-range x in λ_o .

the constraints

$$w_j \geq w_{j+1} \geq 0, \quad j = 1, \dots, N-1, \quad \sum_{j=1}^N w_j^2 = 1.$$

Without weight optimization the images are noisy, with spurious peaks. We illustrate this in Figure 6.2, where we plot $\mathcal{I}(\mathbf{x}; \mathbf{w})$ with uniform weights $w_j = 1/\sqrt{N}$, for $j = 1, \dots, N$. The image in the left plot is in a waveguide with perturbed boundary and array at range $z_{\mathcal{A}} = 100\lambda_o$. The image in the right plot is in a waveguide with perturbed medium and array at range $z_{\mathcal{A}} = 50\lambda_o$. Both images are noisy. The results in Figure 4.1 predict that half of the modes remain coherent at $z_{\mathcal{A}} = 100\lambda_o$ in the waveguide with perturbed boundaries ($\mathcal{S}_j > 100\lambda_o$ for $j = 1, \dots, N/2$). Therefore the image is not bad, and can be improved further by the optimization, as shown below. The results in Figure 4.2 show that all the modes are almost incoherent at $z_{\mathcal{A}} = 50\lambda_o$ in the waveguide with perturbed medium ($\mathcal{S}_j < 70\lambda_o$ for $j = 1, \dots, N$). The image is noisy, with prominent spurious peaks, and cannot be improved by optimization, as shown below.

We show in Figures 6.3-6.5 the results of the optimization in a waveguide with perturbed boundary and array at ranges $z_{\mathcal{A}} = 50\lambda_o$, $100\lambda_o$ and $150\lambda_o$. The local average of the image in (6.1) is over an interval of length λ_o in range and of length λ_o , $1.5\lambda_o$ and $2\lambda_o$ in cross-range, respectively. The weights obtained with the numerical optimization are in reasonable agreement with those predicted by the theory. The resolution of the images deteriorates as we increase $z_{\mathcal{A}}$ because more of the higher indexed modes become incoherent.

Figures 6.6-6.7 show the results in a waveguide with perturbed medium and array at ranges $z_{\mathcal{A}} = 25\lambda_o$ and $50\lambda_o$. Here there is no trade-off between resolution and robustness of the image, because most modes lose coherence on roughly the same range scale. Coherent imaging can be done at range $z_{\mathcal{A}} = 25\lambda_o$, and the numerical weights agree with those predicted by the theory. However, at range $z_{\mathcal{A}} = 50\lambda_o$ the

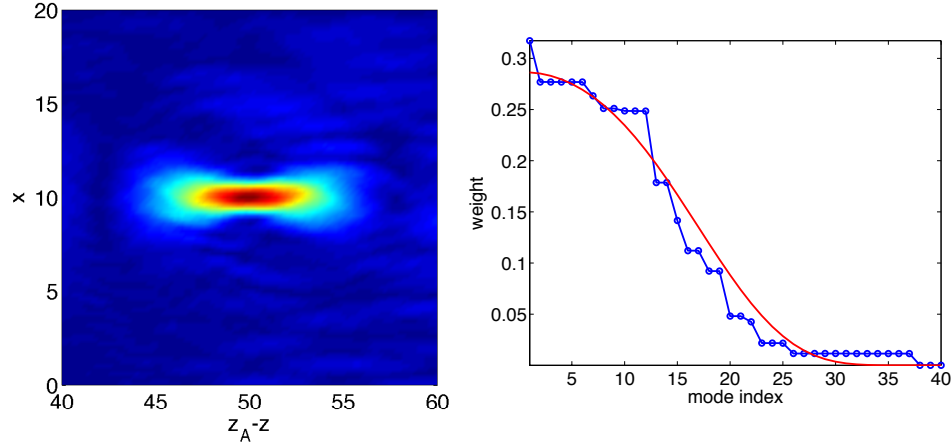


FIG. 6.3. Waveguide with perturbed boundary and array range $z_A = 50\lambda_o$. Left: Image with the numerically computed weights. The abscissa is $z_A - z$ in λ_o and the ordinate is the cross-range x in λ_o . Right: Theoretical weights (in red) and numerical ones (in blue) vs. mode index.

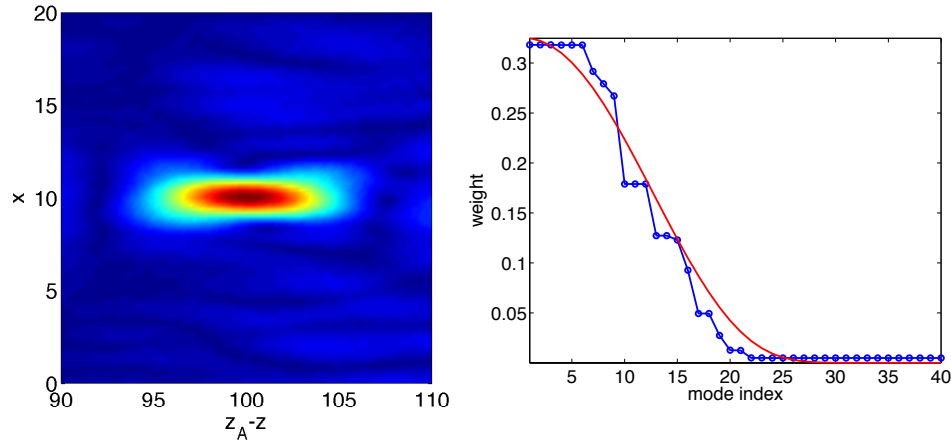


FIG. 6.4. Waveguide with perturbed boundary and array range $z_A = 100\lambda_o$. Left: Image with the numerically computed weights. The abscissa is $z_A - z$ in λ_o and the ordinate is the cross-range x in λ_o . Right: Theoretical weights (in red) and numerical ones (in blue) vs. mode index.

optimization fails to improve the image.

7. Summary. We have carried out a comparative theoretical and numerical study of wave scattering in two types of random waveguides with bounded cross-section: waveguides with random inhomogeneities in the bulk medium and waveguides with random perturbations of the boundary. The wave field is a superposition of waveguide modes with random amplitudes. Coherent imaging relies on the coherent part of the amplitudes, their expectation. However, this decays with the distance of propagation due to cumulative scattering at the random inhomogeneities and boundary perturbations. The incoherent part of the amplitudes, the random fluctuations gain strength and become dominant at long ranges.

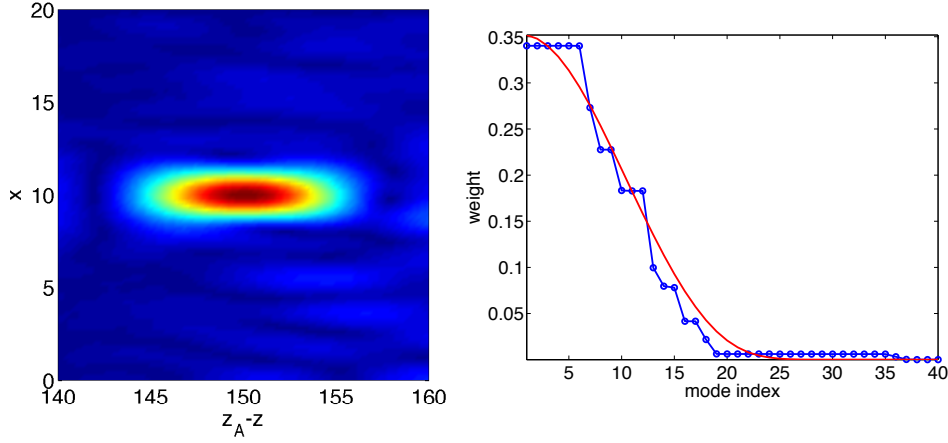


FIG. 6.5. Waveguide with perturbed boundary and array range $z_A = 150\lambda_o$. Left: Image with the numerically computed weights. The abscissa is $z_A - z$ in λ_o and the ordinate is the cross-range x in λ_o . Right: Theoretical weights (in red) and numerical ones (in blue) vs. mode index.

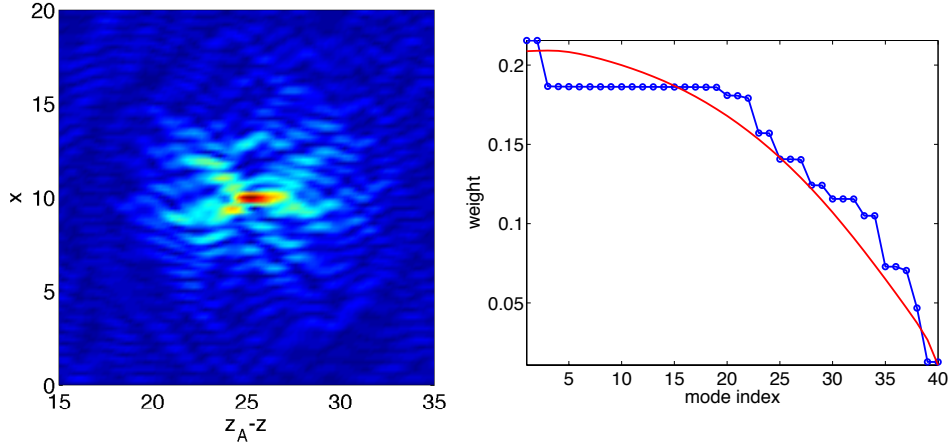


FIG. 6.6. Waveguide with perturbed medium and array range $z_A = 25\lambda_o$. Left: Image with the numerically computed weights. The abscissa is $z_A - z$ in λ_o and the ordinate is the cross-range x in λ_o . Right: Theoretical weights (in red) and numerical ones (in blue) vs. mode index.

The characteristic range scales of decay of the coherent part of the mode amplitudes are called scattering mean free paths. They are frequency and mode-dependent, and they decrease monotonically with the mode index. In waveguides with random boundaries the mode dependence is very strong. Thus, we can image with an adaptive approach that detects and suppresses the incoherent modes in the data in order to improve the image. The high indexed modes are needed for resolution but they are the first to become incoherent. Thus, there is a trade-off between the resolution and robustness of the image, which leads naturally to an optimization problem solved by the adaptive approach. It maximizes a measure of the quality of the image by weighting optimally the mode amplitudes.

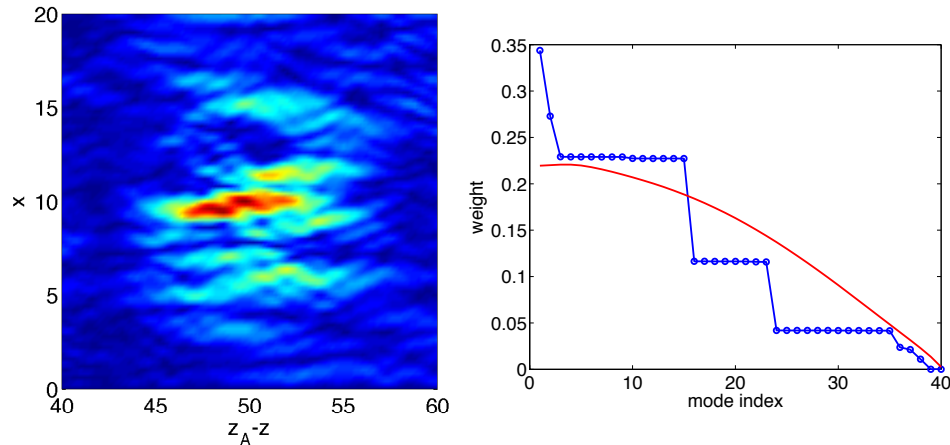


FIG. 6.7. Waveguide with perturbed medium and array range $z_A = 50\lambda_o$. Left: Image with the numerically computed weights. The abscissa is $z_A - z$ in λ_o and the ordinate is the cross-range x in λ_o . Right: Theoretical weights (in red) and numerical ones (in blue) vs. mode index.

Such mode filtering does not work in waveguides with random media because there the modes have similar scattering mean free paths. All the modes become incoherent at essentially the same propagation distances and incoherent imaging should be used instead. There is a large range interval between the scattering mean free paths of the modes and the equipartition distance, where incoherent imaging can succeed. The equipartition distance is the characteristic range scale beyond which the energy is uniformly distributed between the modes, independent of the initial state. The waves lose all information about the source at this distance and imaging becomes impossible.

Incoherent imaging is not useful in waveguides with random boundaries because the equipartition distance is almost the same as the scattering mean free paths of the low indexed modes. Once the waves become incoherent all imaging methods fail.

Acknowledgements. We would like to thank Dr Adrien Semin for carrying out the numerical simulations with Montjoie. The work of L. Borcea was partially supported by the AFSOR Grant FA9550-12-1-0117, the ONR Grant N00014-12-1-0256 and by the NSF Grants DMS-0907746, DMS-0934594. The work of J. Garnier was supported in part by the ERC Advanced Grant Project MULTIMOD-267184. The work of C. Tsogka was partially supported by the European Research Council Starting Grant Project ADAPTIVES-239959.

Appendix A. Numerical simulations of the array data.

In the numerical simulations the source is supported in a disk of radius $\lambda_o/10$, and it emits a pulse

$$f(Bt) = \text{sinc}(Bt) \quad (\text{A.1})$$

modulated by the carrier signal $\cos(\omega_o t)$. The array has $N_R = 39$ receivers located at $\mathbf{x}_r = (x_r, z_A)$, with $x_r = r\lambda_o/2$, $r = 1, \dots, 39$.

The wave propagation in waveguides with perturbed media is simulated by solving the wave equation as a first order velocity-pressure system with the finite element method described in [9]. It is a second order discretization scheme in space and time,

and in the simulations we used spatial mesh size $h = \lambda_o/50$ in cross-range and range, and time discretization step determined by the CFL condition $\Delta t = h/(\sqrt{2}c_{max})$, with c_{max} the maximal value of the speed of propagation in the medium.

The wave propagation in waveguides with perturbed pressure release boundary is simulated by solving the wave equation as a first order velocity-pressure system with the code Montjoie (<http://montjoie.gforge.inria.fr/>). In the simulations we used 8–th order finite elements in space and 4–th order finite differences in time, with spatial mesh size $h = \lambda_o/4$ and time discretization step $\Delta t = 5 \cdot 10^{-6}$ s.

In both cases we use two perfectly matched layers (PML) to the left and right of the computational domain to model the unbounded waveguide in z .

REFERENCES

- [1] R. Alonso, L. Borcea, and J. Garnier, Wave propagation in waveguides with random boundaries, *Commun. Math. Sci.*, 11, 2012, 233-267.
- [2] L. Borcea and J. Garnier, Paraxial coupling of propagating modes in three-dimensional waveguides with random boundaries, arXiv preprint arXiv:1211.0468, 2012.
- [3] L. Borcea, L. Issa, and C. Tsogka, Source localization in random acoustic waveguides, *SIAM Multiscale Modeling Simulations*, 8, 2010, 1981-2022.
- [4] L. B. Dozier and F. D. Tappert, Statistics of normal mode amplitudes in a random ocean, *J. Acoust. Soc. Am.*, 63, 1978, 353-365; *J. Acoust. Soc. Am.*, 63, 1978, 533-547.
- [5] J.-P. Fouque, J. Garnier, G. Papanicolaou, and K. Sølna, *Wave propagation and time reversal in randomly layered media*, Springer, New York, 2007.
- [6] J. Garnier and G. Papanicolaou, Pulse propagation and time reversal in random waveguides, *SIAM J. Appl. Math.*, 67, 2007, 1718-1739.
- [7] C. Gomez, Wave propagation in shallow-water acoustic random waveguides, *Commun. Math. Sci.*, 9, 2011, 81-125.
- [8] W. Kohler and G. Papanicolaou, Wave propagation in randomly inhomogeneous ocean, in *Lecture Notes in Physics*, Vol. 70, J. B. Keller and J. S. Papadakis, eds., Wave Propagation and Underwater Acoustics, Springer Verlag, Berlin, 1977.
- [9] E. Bécache, P. Joly and C. Tsogka, An analysis of new mixed finite elements for the approximation of wave propagation problems, *SIAM J. on Numer. Anal.*, 37, 2000, 1053-1084.